Supplementary Material

1 Model description & modifications implemented

The RAMS-ICLAMS model incorporates a comprehensive two-moment bulk microphysics scheme that resolves the formation and growth of 8 hydrometeor types: cloud droplets, drizzle, rain, (pristine) cloud ice, snow, snow aggregates, graupel and hail (Walko et al., 1995, Meyers et al., 1997). By assuming a generalized Gamma size distribution $f_{\Gamma}(D)$:

$$f_{\Gamma}(D) = \frac{1}{\Gamma(D)} \cdot \left(\frac{D}{D_n}\right)^{\nu-1} \cdot \frac{1}{D_n} \exp\left[-\left(\frac{D}{D_n}\right)\right], \quad (1)$$

where D is the hydrometeor diameter, D_n is the characteristic (scale) hydrometeor diameter, ν is the shape parameter of the distribution, and Γ representing the gamma function, the model prognoses the properties of each hydrometeor type, such as the mass mixing ratio, number concentration and diagnoses the mean mass diameter. The cloud droplet nucleation by aerosols that act as CCN is described by various algorithms such as Saleeby and Cotton (2004), Fountoukis and Nenes (2005) and Saleeby and van den Heever (2013). These formulations consider the local meteorology (temperature, supersaturation, updraft velocity) and aerosol chemistry (concentration, size, solubility). The microphysics scheme of RAMS-ICLAMS includes sink terms for airborne aerosols, such as nucleation scavenging, wet and dry deposition. Aerosols are also allowed to be regenerated upon hydrometeor evaporation/sublimation, and to undergo secondary activation with clouds. This is achieved by number and mass tracking routines in the model.

The microphysics scheme of RAMS-ICLAMS describes the most important hydrometeor interactions, which are summarized in Table S1.

Table S1: Configuration of the RAMS-ICLAMS modeling system

Microphysical Process	Parameterization
Cloud droplet autoconversion & accretion	Tzivion et al., 1987
Heterogenous ice nucleation	Meyers et al., 1992; DeMott et al., 2010
Homogenous freezing of cloud droplets	DeMott et al., 1994
Contact freezing of cloud droplets	Meyers et. Al., 1992
Riming of cloud & drizzle droplets	Saleeby and Cotton, 2008
Heat & vapor diffusion	Walko et al., 2000
Hydrometeor sedimentation	Feingold et al.,1998
Shedding & melting	Walko et al., 1995, Meyers et al., 1997
Ice Aggregation	Walko et al., 1995, Meyers et al., 1997

Each possible interaction of hydrometeor pairs is explicitly resolved by the microphysics scheme. The number concentration loss rate $\frac{dN_{tx}}{dt}$ of hydrometeor x, with number concentration N_{tx}, which is collected by a hydrometeor y, with number concentration N_{ty} is given by:

$$\frac{dN_x}{dt} = \frac{N_{tx}N_{ty}\pi F_\rho}{4}\int_0^\infty\int_0^\infty dD_x dD_y \cdot \left\{\left(D_x + D_y\right)^2\left|u_{tx}(D_x) - u_{ty}\left(D_y\right)\right|f_{\Gamma x}(D_y)f_{\Gamma y}(D_y))E(x,y)\right\}, \quad (2)$$

And similarly, the mass concentration loss by:

$$\frac{dr_x}{dt} = -\frac{N_{tx}N_{ty}\pi F_\rho}{4\rho_\alpha}\int_0^\infty\int_0^\infty dD_x dD_y \cdot m(D_x)\left\{\left(D_x + D_y\right)^2\left|u_{tx}(D_x) - u_{ty}\left(D_y\right)\right|f_{\Gamma x}(D_y)f_{\Gamma y}(D_y)E(x,y)\right\}, \quad (3)$$

where F_ρ being a density factor, ρ_α the air density, $E(x,y)$ the collection of the hydrometeor pair and $u_{tx}(D_x) = a_x(D_x)^{\beta_x}$ the terminal velocity of hydrometeor x, (α_x, β_x parameters). Verlinde et al. (1990) provided both an analytical solution and a numerical framework, by replacing the integration terms with the collection tables for number $J_c\left[(x,y), D_{nx}, D_{ny}\right]$ and mass change $J_r\left[(x,y), D_{nx}, D_{ny}\right]$, that are precomputed into look-up tables. The equations above simplify to:

$$\frac{\Delta N_x}{\Delta t} = -\frac{N_{tx}N_{ty}\pi F_\rho E(x,y)}{4} \cdot J_c\left[(x,y), D_{nx}, D_{ny}\right], \quad (4)$$

and

$$\frac{\Delta r_x}{\Delta t} = -\frac{N_{tx}N_{ty}\pi F_\rho E(x,y)}{4\rho_a} \cdot J_r\left[(x,y), D_{nx}, D_{ny}\right], \tag{5}$$

The concept of collection efficiency is very important the development of secondary ice mechanisms relies upon it, as described in the following sections.

1.1 Secondary ice production through rime splintering

The rime splintering or Hallett-Mossop (HM) is the only SIP mechanism included in the original microphysics scheme of RAMS-ICLAMS. The parameterization of HM is developed by Cotton et al. (1986) based on the experimental results of Hallett and Mossop (1974). It predicts the production rate of ice splinters (resolved as cloud ice particles by the model) when cloud or drizzle droplets are collected by snow, aggregates, graupel or hail particles. The production rate $\frac{dN}{dt}$ is given by:

$$\log_{10}\left(\frac{dN/dt}{N_L}\right) = (0.93\log_{10} N_s - 6.0)\, f_1\,(T_s), \tag{6}$$

Where N_s (N_L) are the collection rates of cloud/drizzle droplets smaller (larger) than 24μm in diameter. The efficiency of HM peaks at -5°C and is zero for temperatures $T_s(°\mathrm{C})$ less than -8°C or greater than -3°C, which is described by the linear interpolating function:

$$f_1(T_s) = \begin{cases} (T_s - 5)/2\,; & -5 < T_s < -3 \\ (T_s - 5)/3; & -8 < T_s < -5\,, \\ 0\,; & else \end{cases} \tag{7}$$

1.2 Secondary ice production through ice-ice collisions

The production of secondary ice due to the collisions of pre-existing ice hydrometeors (collisional break-up, CBR) is the first of the three newly implemented SIP mechanisms. The approach used to incorporate CBR follows the methodology described by Sotiropoulou et al. (2021a, Appendix B), adapted here for the RAMS–ICLAMS microphysics scheme. Among the five ice hydrometeors, all 15 (including self-collection) collision pairs are resolved, and the resulting number and mass transfers are calculated based on Eq. 4-5. It is assumed that every pair can result in ice multiplication, except for cloud ice – cloud ice collisions, due to their small size and their inefficiency of rimming. As mentioned in the previous sections, the formulation of Phillips et al. (2017a) is being adapted for the calculation of secondary ice production rate per collision, which is derived by considering the collisional kinetic energy (CKE) of falling hydrometeors as the main driver of the CBR process. This formulation relies on previous experimental results of Vardiman (1978) and Takahashi et al. (1995). The number N_{CBR} of secondary ice particles generated is calculated by:

$$N_{CBR} = aA\left(1 - exp\left\{-\left[\frac{CK_0}{aA}\right]^{\gamma}\right\}\right), \tag{8}$$

where $K_0 = \frac{1}{2}\frac{m_1 m_2}{m_1+m_2}(\Delta u_{n12})^2$ is the initial kinetic energy of the collision pair, $m_{1,2}$ the masses of each hydrometeor and $a = \pi D^2$ the surface area of the smaller hydrometeor. The term Δu_{n12} represents the difference of terminal velocities between the colliding hydrometeors and is calculated by $|\Delta u_{n12}| = \{(1.7u_{n1} - u_{n2})^2 + 0.3u_{n1}u_{n2}\}^{1/2}$, as proposed by Mizuno et al. (1990) and Reisner et al. (1998), to account for systematic underestimation of the kinetic energy, when $u_{n1} \approx u_{n2}$. Furthermore, A represents the number density of breakable asperities on the surfaces of hydrometeors, with with $\Psi < 0.5$ being the rimmed fraction of the most fragile ice particle and β, σ and γ are empirical constants depending on the type of colliding pairs, presented on Table S2. For graupel/hail-graupel/hail collisions $A = \frac{a_0}{3} + \max\left(\frac{2a_0}{3} - \frac{a_0}{9}|T - T_0|, 0\right)$ and $A = \beta(1 + 100\Psi^2)\left(1 + \frac{\sigma}{D^{1.5}}\right)$ for all other types, with $T_0 = -15°\mathrm{C}$ and a_0 an empirical constant, listed in Table S2. Lastly C is the asperity-fragility coefficient which also depends on the collision type. The parameterization of Phillips et al. (2017a) is designed for particles with diameters in the range $500\mu m < D < 5mm$. Nevertheless, they suggest that it can be extended to particle sizes outside this interval by constraining the input variables to the nearest limit of the prescribed range. The maximum number of predicted fragments per collision N_{max} is capped at 100 for all collisions, except for hail-hail collisions, where it is set to 10^3. Moreover, the fraction of initial fragment mass to mass of the parent (more fragile) particle ζ is set to 10^{-6} for hail-hail collisions and 10^{-3} for all other pairs. These constraints arise for the experimental result of Vardiman (1978) and Phillips et al. (2017a). Gautam et al. (2024) have updated the values of β and C and introduced ramp shape functions for ζ and Ψ regarding the snow/aggregate collisions with graupel and hail, to improve consistency with the newly available experimental data, presented in Table S3. It should also be noted that the schemes of Phillips et al. (2017a) and Gautam et al. (2024), direct the produced fragments to the categories of cloud ice or snow based on their size. However, in RAMS-ICLAMS all predicted fragments produced by CBR are transferred to the cloud ice category. Additionally, since the model doesn't explicitly track the rimmed mass on each hydrometeor, a constant value $\Psi = 0.25$ is assumed.

Using Eq.4-5 for the collection rates, the total number of emitted ice fragments $\frac{\Delta N_i^{CBR}}{\Delta t}$, and their mass transferred by the parent hydrometeor, is computed by multiplying the fragments generated per collision by the complementary fraction of particles, meaning those involved in collisions that do not result in collection.

Hence:

$$\frac{\Delta N_i^{CBR}}{\Delta t} = \frac{N_{tx} N_{ty} \pi F_\rho}{4} \cdot [1 - E(x,y)] \cdot J_c\big[(x,y), D_{nx}, D_{ny}\big] \cdot N_{CBR}, \tag{9}$$

and

$$\frac{\Delta r_i^{CBR}}{\Delta t} = \frac{N_{tx} N_{ty} \pi F_\rho}{4 \rho_a} \cdot [1 - E(x,y)] \cdot J_r\big[(x,y), D_{nx}, D_{ny}\big] \cdot \zeta, \tag{10}$$

It should be stated that collisions of cloud ice with larger ice particles do not lead to mass transfer to secondary ice, so Eq.10 will not apply in this case.

Table S2: Parameters of the CBR scheme for each collision type by Phillips et al. (2017a)

Parameter	Type Ia	Type Ib	Type IIa	Type IIb
$\boldsymbol{C}$ ($\boldsymbol{J^{-1}}$)	$6.30 \times 10^6 \times \psi$	3.31×10^5	$6.09 \times 10^6 \times \psi$	$7.08 \times 10^6 \times \psi$
$\boldsymbol{\gamma}$	0.30	0.54	$0.50 - 0.25 \times \Psi$	$0.50 - 0.25 \times \Psi$
$\boldsymbol{\beta}$	–	–	1.41×10^6	1.58×10^7
$\boldsymbol{\sigma}$	–	–	3.98×10^6	1.33×10^{-4}
$\boldsymbol{\psi}$	3.50×10^{-3}	3.50×10^{-3}	3.50×10^{-3}	3.50×10^{-3}
$\boldsymbol{\zeta}$	10^{-3}	10^{-6}	10^{-3}	10^{-3}
$\boldsymbol{\alpha_0}(\boldsymbol{m^{-2}})$	$3.78 \times 10^4 \times \left(1 + \frac{0.0079}{D^{1.5}}\right)$	4.35×10^5	–	–

Type Ia: Collisions of Graupel with Graupel/Hail, Type Ib: Collisions of Hail-Hail, Type IIa: Collisions of Snow (Dendrites) with all other ice particles, Type IIb: Collisions of Snow (Spatial planar) with all other ice particles.

Table S3: Updated parameters of the CBR scheme for Type IIa,b by Gautam et al. (2024)

Parameter	**Attributes**
$\boldsymbol{\beta(m^{-2}) = 1.41 \times 10^{7}}$	*Type IIa*
$\boldsymbol{C\,(J^{-1}) = 8.03 \times 10^{7}}$	
$\boldsymbol{\beta(m^{-2}) = 1.41 \times 10^{7}}$	*Type IIb*
$\boldsymbol{C\,(J^{-1}) = 8.03 \times 10^{7}}$	
$\chi = \begin{cases} \chi_1 = 0.1 & D < D_0 \\ \left(\dfrac{\chi_1 - \chi_0}{D_1 - D_0}\right)(D - D_0) + \chi_1 & D_0 < D < D_1 \\ \chi_0 = 0.3 & D > D_1 \end{cases}$	*Empirical constants:* $\boldsymbol{D_0 = 4.5 \times 10^{-4} m, D_1 = 9.0 \times 10^{-4} m}$
$\zeta = \chi^{3}$	
$\Psi = \begin{cases} 0 & D < D_3 \\ \left(\dfrac{D - D_3}{D_4 - D_3}\right)\Psi_1 & D_3 < D < D_4 \\ \Psi_1 & D > D_4 \end{cases}$	*Empirical constants:* $\boldsymbol{D_3 = 3.0 \times 10^{-4} m, D_4 = 2.0 \times 10^{-3} m}$ $\boldsymbol{\Psi_1 = 0.30}$ *(Type IIa),* $\boldsymbol{\Psi_1 = 0.18}$ *(Type IIb)*

1.3 Secondary ice production through droplet shattering

RAMS-ICLAMS computes hydrometeor number and mass transfer for rain–ice collisions using Eq. 4–5, applying the required modifications for each hydrometeor pair. The destination category of the transferred mass and number depends on the interacting hydrometeor types. For instance, collisions between rain droplets and cloud (pristine) ice produce mass and number transfer to the hail category, following Ferrier (1994). Similarly, collisions of rain with snow or aggregates may transfer mass and number to snow, aggregates, graupel, or hail, depending on the density of the coalesced particles. Rain–graupel collisions are routed to either the graupel or hail category, also based on the computed density of the coalesced particles, following Milbrandt and Yau (2005a,b). Finally, rain–hail collisions transfer mass directly from rain to hail. Rain droplets may also interact with IN particles, resulting in immersion freezing as described by Saleeby and van den Heever (2013).

Droplet shattering (DRS) is the second SIP mechanism integrated into RAMS-ICLAMS. Phillips et al. (2018) examines two modes of initiating the freezing process of raindrops and provides equations for the calculation of the number of generated ice splinters, N_{DS}. In the first mode, a raindrop freezes either by collecting pristine particles or through heterogeneous freezing. In this study, it is assumed that the frozen drop produced by either pathway can subsequently shatter, generating multiple ice fragments. The number of fragments is parameterized following Phillips et al. (2018). The formulation is obtained by fitting a range of laboratory datasets to a Lorentzian function of temperature combined with a polynomial dependence on drop size. Specifically, the total number of fragments (N) produced per frozen drop is given by:

$$N = \Xi(D_r)\Omega(T)\left[\frac{\zeta\eta^2}{(T-T_0)^2+\eta^2} + \beta T\right], \tag{11}$$

where D_r (mm) is the diameter of the freezing rain droplet, $T(K)$ is the air temperature, T_0, η, β and ζ are parameters of the Lorentzian function, and Ξ, Ω represent cubic interpolating functions. Equation 11 applies to rain droplet diameters $D_r < 1.6\ mm$; for larger droplets, linear extrapolation is required. However, N represents the sum of big fragments N_B, which are transferred to hail category in the model, and tiny splinters N_T, which are transferred to pristine ice.

The number of big fragments is calculated by the following expression:

$$N_B = \min\left\{N, \Xi(D_r)\Omega(T)\left[\frac{\zeta_B\eta_B^2}{\left(T-T_{B,0}\right)^2+\eta_B^2}\right]\right\}, \tag{12}$$

where $T_{0,B}, \eta_B$ and ζ_B are parameters of this new Lorentzian function. Thus, the number of tiny ice fragments is $N_T = N - N_B$.

The second mode of DRS arises from the accretion of rain droplets upon impact with larger ice particles, such as snow, aggregates, graupel and hail. Phillips et al. (2018) calculate the number of tiny splinters ejected during such collisions, with the following empirical, energy-based equation:

$$N_{DRS} = 3\Phi(T) \times [1 - f(T)] \times \max(DE - DE_{crit}, 0), \tag{13}$$

where $DE = K_0/S_e$ is a dimensionless energy factor, representing the ratio of initial kinetic energy K_0 (discussed in the previous section) over the surface energy S_e, which in turn is expressed by $S_e = \gamma_{liq}\pi D_r^2$, where $\gamma_{liq} = 0.073\ J\ m^{-2}$ is the surface tension of liquid water. The critical value of DE, $DE_{crit} = 0.2$, is the lowest threshold for the splashing of the rain droplet to occur, during the collision. The parameter $f(T) = -c_w T/L_f$ denotes the initial fraction of a supercooled raindrop that freezes during the first stage of the freezing process. Here, $c_w = 4.2\ kJ(kg)^{-1}K^{-1}$ is the specific heat capacity of liquid water, $L_f = 3.3 \times 10^5 J(kg)^{-1}$ is specific latent heat of freezing, and $T(°C)$ is the raindrop's initial freezing temperature. The empirical factor $\Phi(T) = \min\{4f(T), 1\}$ represents the probability that any new droplet formed in the splash products contains a frost-induced secondary ice particle. It is also estimated that the ratio of the mass of the newly formed splinters over the initial mass of the raindrop is $\zeta = 10^{-3}$, per collision. Hence, the transfer equations for DRS are modified as:

$$\frac{\Delta N_i^{DRS}}{\Delta t} = \frac{N_{tr} N_{ty} \pi F_\rho}{4} \cdot [1 - E(x,y)] \cdot J_c\left[(x,y), D_{nx}, D_{ny}\right] \cdot N_{DRS}, \tag{14}$$

and

$$\frac{\Delta r_i^{DRS}}{\Delta t} = \frac{N_{tr} N_{ty} \pi F_\rho}{4 \rho_a} \cdot [1 - E(x,y)] \cdot J_r\left[(x,y), D_{nx}, D_{ny}\right] \cdot \zeta, \tag{15}$$

where N_{tr}, N_{ty} represent the number concentrations of rain droplets and the ice hydrometeor, respectively.

1.4 Secondary ice production through ice sublimation

Sublimation breakup (SUBBR) is the third SIP mechanism newly included the microphysics scheme of the model, and it is based on the formulation of Deshmukh et al. (2022). For each snow-aggregate particle undergoing sublimation, the number of fragments produced $\left(\frac{d\tilde{N}_{SUBBR}}{dt}\right)$ is calculated by:

$$\frac{d\tilde{N}_{SUBBR}}{dt} = \beta D_n^{\gamma+1} \times (100 - RH_i) f_u \Xi \nu, \tag{16}$$

where $\beta = 0.0157$and $\gamma = -0.55$are fitting parameter, D_n is the diameter of the hydrometeor, RH_i represents the relative humidity with respect to ice, and $f_u = 0.78 + 0.308 N_{sc}^{\frac{1}{3}} N_{Re}^{\frac{1}{2}}$ is the ventilation coefficient for vapor diffusion, as proposed by Pruppacher and Klett, (1997), N_{sc}, $N_{Re}$are the Schmidt and Reynolds numbers respectively. Lastly, Ξ and ν are empirical factors that are expressed as cubic interpolation functions of the hydrometeor diameter and relative humidity over ice, that determine the threshold above which sublimation breakup can occur. A similar equation is valid for the secondary ice produced by larger and heavily rimmed sublimating particles, like graupel and hail:

$$\frac{d\tilde{N}_{SUBBR}}{dt} = \left(\frac{\rho_{D0}}{\rho_r}\right) \beta D_n^{\gamma+1} \times (100 - RH_i) f_u \Xi \nu^*, \tag{17}$$

The empirical parameters in the sublimation breakup scheme are calibrated to reproduce fragmentation rates, that match the observations from Dong et al. (1994). The first term represents a density-correction factor, where ρ_r is the density of the sublimating particle (graupel-hail) and $\rho_{D0} = 300 kg/m^3$ the density of particles in the experiments of Dong et al. (1994). Since graupel and hail particles span across a wide density range, the scheme introduces this density-correction factor to scale breakup rates relative to this laboratory baseline. Lower-density graupel is structurally weaker and thus fragments more readily, while higher-density graupel is mechanically stronger and fragments less. In Eq.17, $\beta = 0.0836$ and v^* is an empirical factor, represented by a modified version of the original cubic interpolation factor for v.

For both smaller and larger ice particles, the ratio χ of sublimated mass over the parent particle mass is:

$$\chi = \psi^{2.3}, \psi = 0.567 \times \exp\left(-\frac{D_n}{0.003815}\right), \tag{18}$$

The valid range for hydrometeor diameters in Eq.18 is $0.25mm < D_n < 8mm$, and for the cubic interpolating functions Ξ, v and v^* is $0.30mm < D_n < 2mm$. If D_r falls outside the valid range, in each case, its value is adjusted to the nearest boundary. Using Eq.16–18, the rate of secondary ice generation via SUBBR, in terms of number concentration and mass, is:

$$\frac{dN_{SUBBR}}{dt} = \frac{d\widehat{N}_{SUBBR}}{dt} \cdot N_{sn}, \tag{19}$$

for the number concentration of cloud ice, and

$$\frac{dM_{SUBBR}}{dt} = r_{sn} \cdot N_{sn} \cdot \chi, \tag{20}$$

where r_{sn}, N_{sn} correspond to the sublimation mixing ratio and the number concentration of every hydrometeor category, respectively. It should be noted that the portion of the sublimated mass dM_{SUBBR} that originally transferred to water vapor is instead reassigned to the cloud-ice category.

2 Supplementary figures

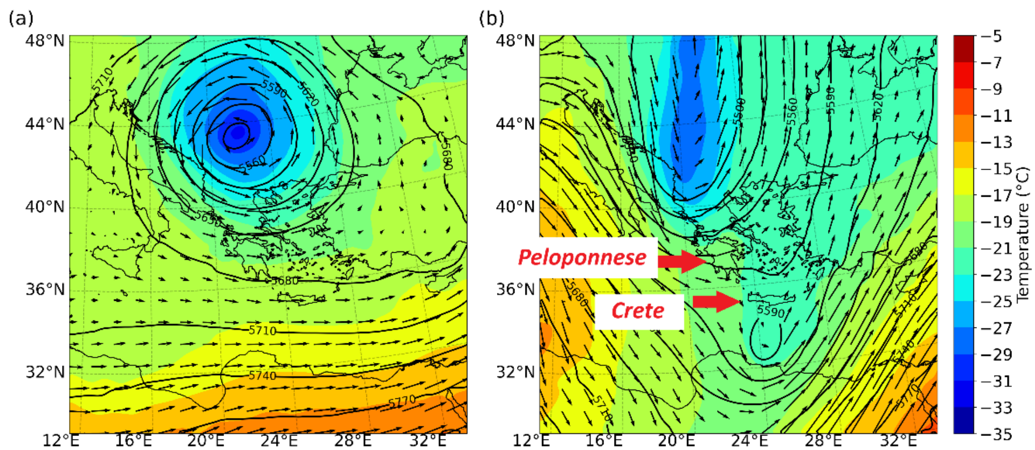

Figure S1: Synoptic conditions on the 500 hPa isobaric surface for (a) the convective case (CC) (11 November 2024, 00 UTC) and (b) the stratiform case (SC) (7 December 2024, 12 UTC). Color shading represents temperature (°C), black contours show geopotential height (m), and wind vectors illustrate the flow field.

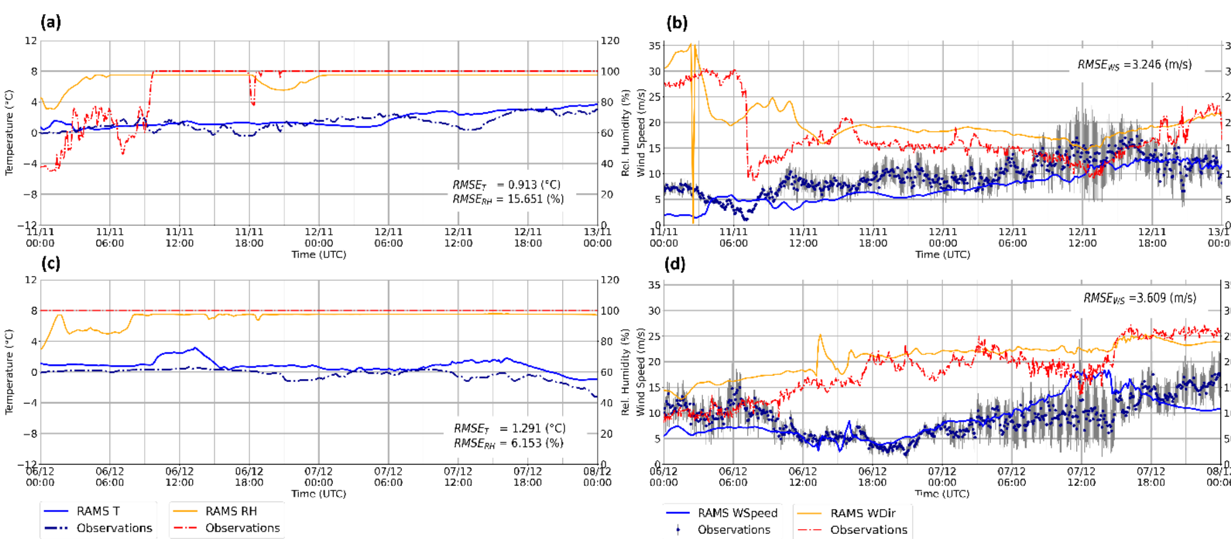

Figure S2: Time series at the (HAC)² station for CC (a, c) and SC (b, d). Panels (a, c) display simulated (solid) and observed (dashed) near surface temperature & relative humidity. Panels (b, d) show simulated wind speed (wspeed) and direction (wdir) (solid) together with observed wind speed (blue markers) and wind direction (dashed) at ~10m AGL. Vertical grey bars indicate the 5-min variance of the observed wind speed.

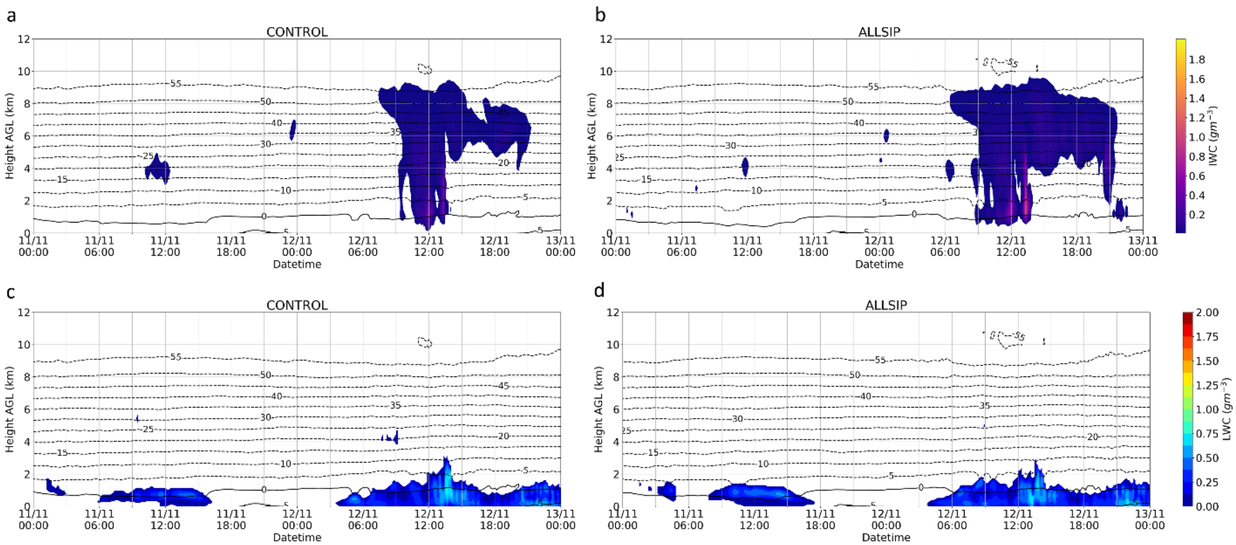

Figure S3: Time–height cross section is centered over the Achilles Base. Time-height cross sections of simulated IWC (g m⁻³) (a, b) and LWC (g m⁻³) (c, d) from the CONTROL (a, c) and ALLSIP (b, d) experiments for the convective case (CC). The data are extracted from the model column overlying the Achilles Base site.

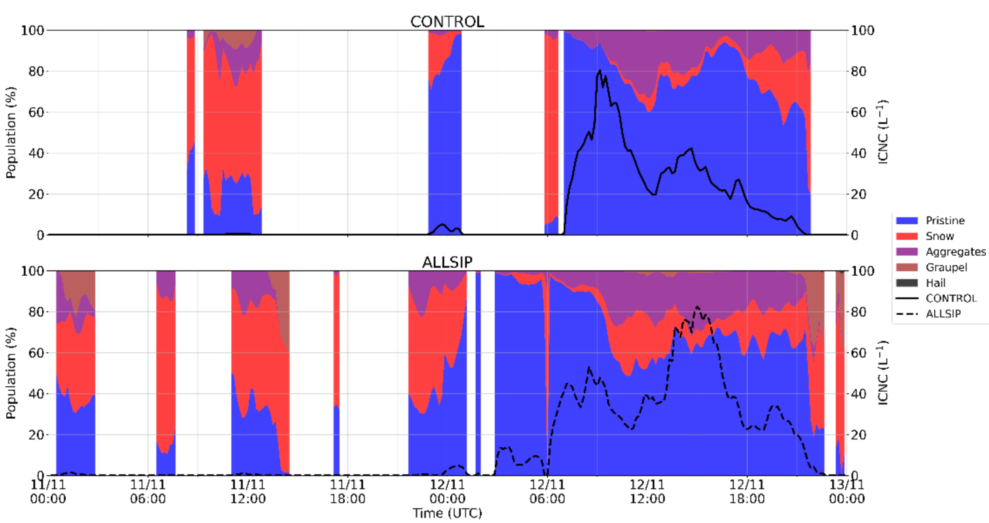

Figure S4: Temporal evolution of the relative contributions of ice hydrometeor populations for the CONTROL (top) and ALLSIP (bottom) simulations, for the convective case (CC). The stacked areas represent the percentage contribution of pristine ice (blue), snow (red), aggregates (purple), graupel (brown), and hail (dark brown) to the ICNC. Only gridcells with non-zero mixing ratio are included, at Achilles Base. The solid and dashed black lines show the corresponding total ICNC for the CONTROL and ALLSIP simulations, respectively, on the secondary y-axis.

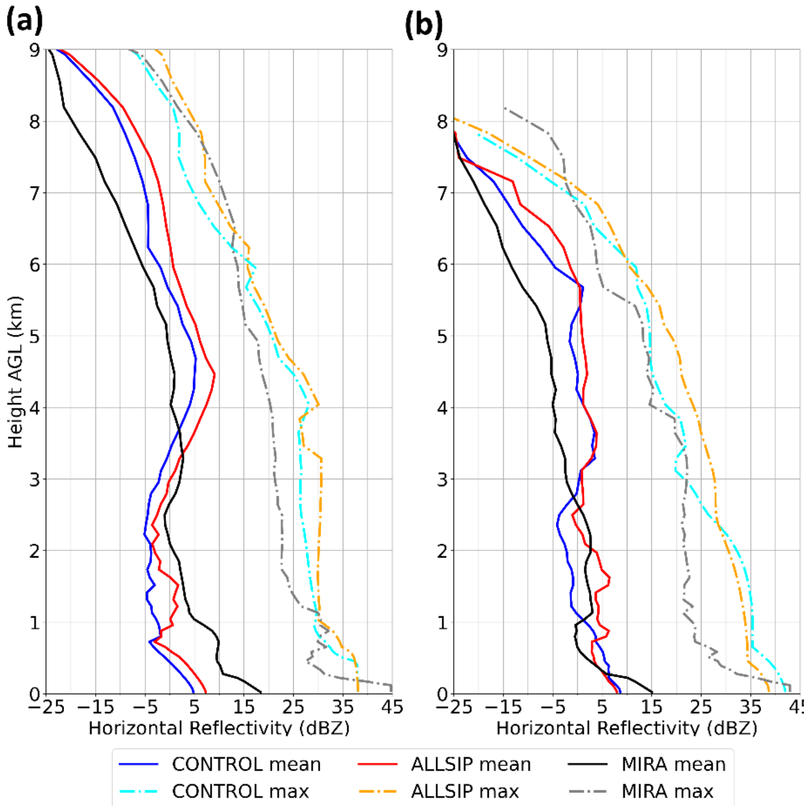

Figure S5: Vertical profiles of reflectivity (dBZ) at Achilles Base for (a) the convective (CC) and (b) the stratiform (SC) case. Solid lines represent the temporal mean over the selected periods of CC and SC, while dashed lines represent the temporal maximum over the same period. Blue (CONTROL), red (ALLSIP), and black (MIRA radar) indicate the mean profiles; cyan, orange, and gray indicate their corresponding maximum profiles.

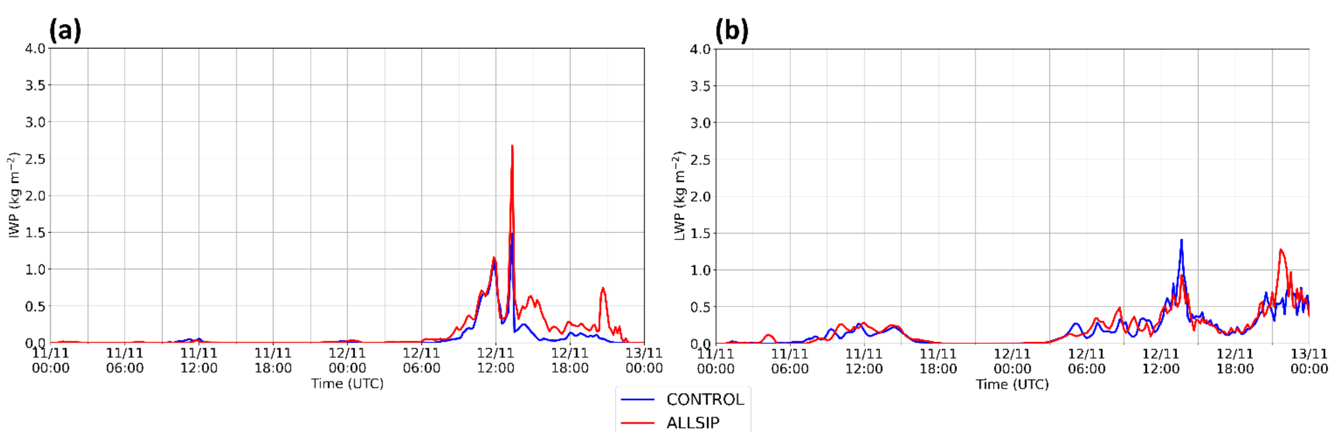

Figure S6: Timeseries of IWP (a) and LWP (b) for the convective case (CC). The blue line represents the CONTROL and the red line the ALLSIP simulations. The water column is integrated over the Achilles Base.

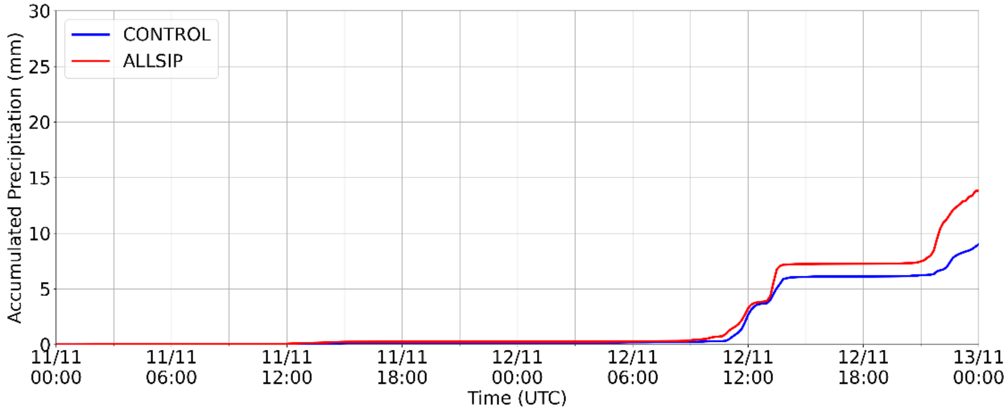

Figure S7: Timeseries of cumulative precipitation at the Achilles Base for the convective case (CC). The blue line represents the CONTROL and the red line the ALLSIP simulations.

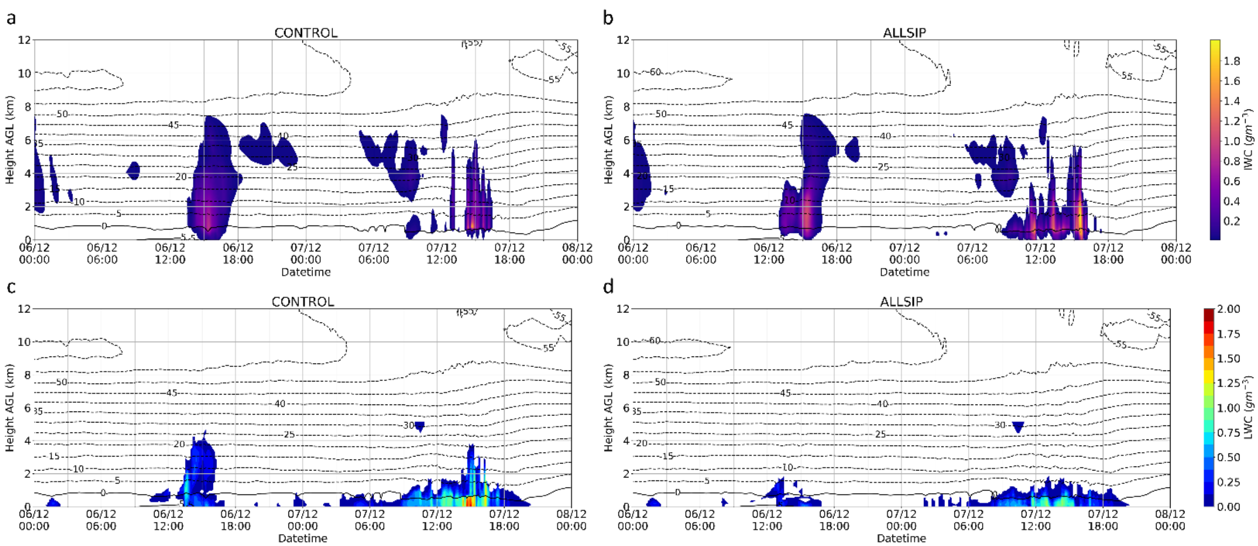

Figure S8: Time-height cross sections of simulated IWC (g m⁻³) (a, b) and LWC (g m⁻³) (c, d) from the CONTROL (a, c) and ALLSIP (b, d) experiments for the stratiform case (SC). The data are extracted from the model column overlying the Achilles Base site.

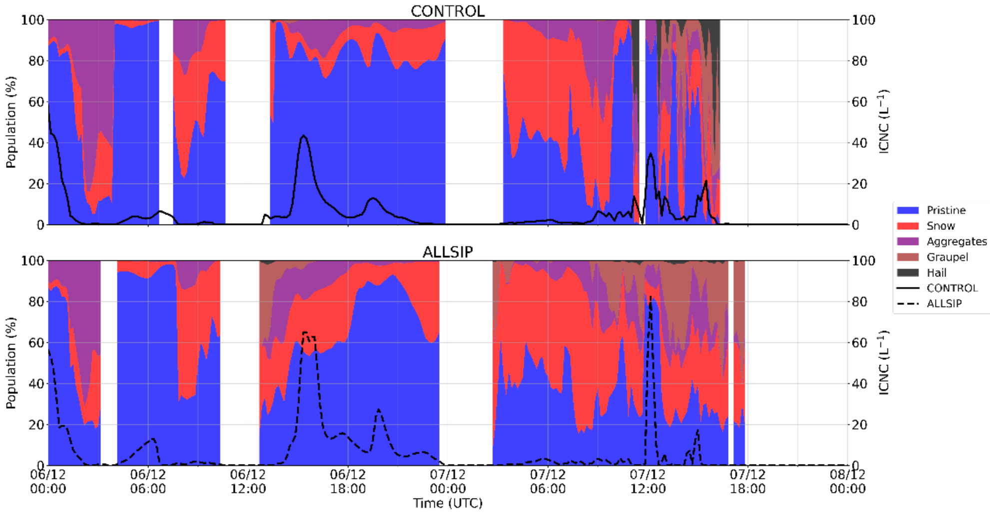

Figure S9: Temporal evolution of the relative contributions of ice hydrometeor populations for the CONTROL (top) and ALLSIP (bottom) simulations, for the stratiform case (SC). The stacked areas represent the percentage contribution of pristine ice (blue), snow (red), aggregates (purple), graupel (brown), and hail (dark brown) to the ICNC. Only gridcells with non-zero mixing ratio are included, at Achilles Base. The solid and dashed black lines show the corresponding total ICNC for the CONTROL and ALLSIP simulations, respectively, on the secondary y-axis.

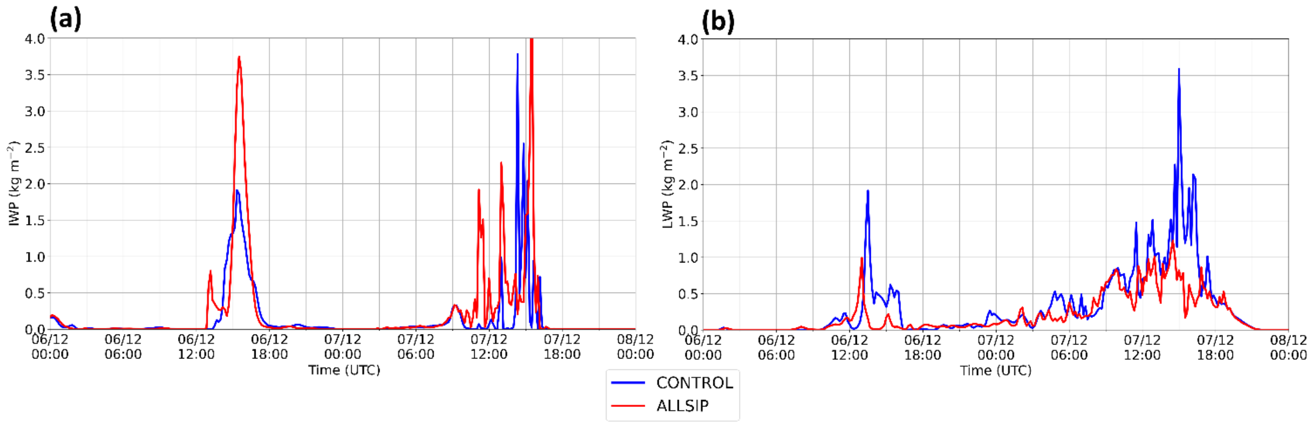

Figure S10: Timeseries of IWP (a) and LWP (b) for the stratiform case (SC). The blue line represents the CONTROL and the red line the ALLSIP simulations. The water column is integrated over the Achilles Base.

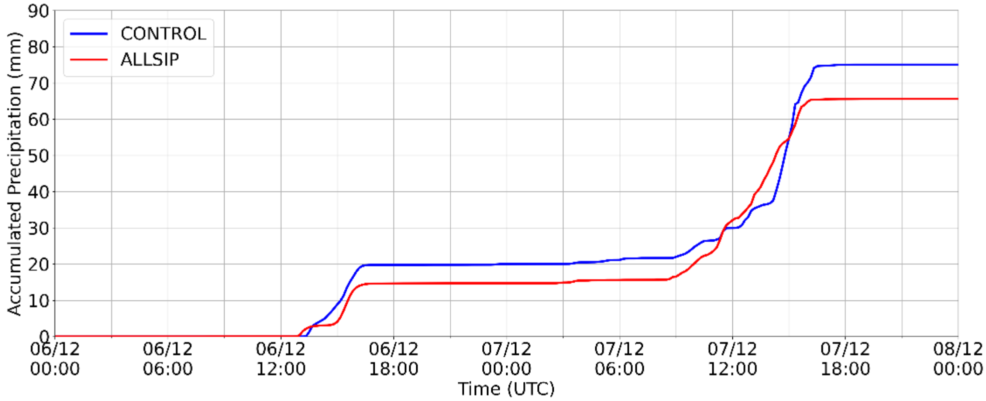

Figure S11: Timeseries of cumulative precipitation at the Achilles Base for the stratiform case (SC). The blue line represents the CONTROL and the red line the ALLSIP simulations.